

# Exploration of Interpretability Techniques for Deep COVID-19 Classification using Chest X-ray Images

**Soumick Chatterjee<sup>1,2,5\*+</sup>, Fatima Saad<sup>4,6+</sup>, Chompunuch Sarasaen<sup>2,4,6+</sup>, Suhita Ghosh<sup>3,5+</sup>, Valerie Krug<sup>3,5</sup>, Rupali Khatun<sup>7,8</sup>, Rahul Mishra<sup>9</sup>, Nirja Desai<sup>10</sup>, Petia Radeva<sup>7,11</sup>, Georg Rose<sup>4,6</sup>, Sebastian Stober<sup>3,5</sup>, Oliver Speck<sup>2,6,12,13</sup>, and Andreas Nürnberger<sup>1,5,13</sup>**

<sup>1</sup>Data and Knowledge Engineering Group, Otto von Guericke University Magdeburg, Germany

<sup>2</sup>Biomedical Magnetic Resonance, Otto von Guericke University Magdeburg, Germany

<sup>3</sup>Artificial Intelligence Lab, Otto von Guericke University Magdeburg, Germany

<sup>4</sup>Institute for Medical Engineering, Otto von Guericke University Magdeburg, Germany

<sup>5</sup>Faculty of Computer Science, Otto von Guericke University Magdeburg, Germany

<sup>6</sup>Research Campus STIMULATE, Otto von Guericke University Magdeburg, Germany

<sup>7</sup>Departament de Matemàtiques i Informàtica, Universitat de Barcelona, Barcelona, Spain

<sup>8</sup>Translational Radiobiology, Department of Radiation Oncology, Universitätsklinikum Erlangen, Erlangen, Germany

<sup>9</sup>Apollo Hospitals, Bilaspur, India

<sup>10</sup>HCG Cancer Centre, Vadodara, India

<sup>11</sup>Computer Vision Center, Cerdanyola, Barcelona, Spain

<sup>12</sup>German Center for Neurodegenerative Diseases, Magdeburg, Germany

<sup>13</sup>Center for Behavioral Brain Sciences, Magdeburg, Germany

\*soumick.chatterjee@ovgu.de

+these authors contributed equally to this work

## ABSTRACT

The outbreak of COVID-19 has shocked the entire world with its fairly rapid spread and has challenged different sectors. One of the most effective ways to limit its spread is the early and accurate diagnosis of infected patients. Medical imaging such as X-ray and Computed Tomography (CT) combined with the potential of Artificial Intelligence (AI) plays an essential role in supporting the medical staff in the diagnosis process. Thereby, five different deep learning models (ResNet18, ResNet34, InceptionV3, InceptionResNetV2, and DenseNet161) and their Ensemble have been used in this paper to classify COVID-19, pneumoniæ and healthy subjects using Chest X-Ray images. Multi-label classification was performed to predict multiple pathologies for each patient, if present. Foremost, the interpretability of each of the networks was thoroughly studied using local interpretability methods - occlusion, saliency, input X gradient, guided backpropagation, integrated gradients, and DeepLIFT, and using a global technique - neuron activation profiles. The mean Micro-F1 score of the models for COVID-19 classifications ranges from 0.66 to 0.875, and is 0.89 for the Ensemble of the network models. The qualitative results depicted the ResNets to be the most interpretable models. This research demonstrates the importance of using interpretability methods to compare different models before making the decision regarding the best-performing model.

## Introduction

In 2020, the world witnessed a serious new global health crisis: the outbreak of the infectious COVID-19 disease, which is caused by the Severe Acute Respiratory Syndrome Coronavirus 2 (SARS-CoV-2)<sup>1,2</sup>. Owing to its long incubation period and its highly contagious nature, it is important to identify the infected cases early and isolate them from the healthy population. So far, viral nucleic acid detection using Reverse Transcription Polymerase Chain Reaction (RT-PCR) has been considered the golden reference standard diagnostic method<sup>3</sup>. However, it was reported that RT-PCR tests suffer from a high rate of false negatives mainly due to laboratory and sample collection errors<sup>4,5</sup>.

On the other hand, medical imaging arises as a tremendous alternative candidate for screening COVID-19 cases and for discriminating them from other conditions, whereas most of the infected patients show abnormalities in medical chest imaging<sup>6-8</sup>. In this context, chest radiography (CXR) and Computed Tomography (CT) have been widely used in front-line hospitals for the diagnosis<sup>9-11</sup>. In some cases, it was shown that chest CT images have exhibited higher sensitivity than RT-PCR and have detected COVID-19 infections in patients with negative RT-PCR results<sup>4,11-13</sup>. However, there are several advantages of fostering the use of CXR imaging in clinical practice, such as faster diagnosis, infection control, and less harmfulness than

CT<sup>14,15</sup>. Moreover, X-ray machines are much more available than CT scanners, especially in developing countries.

Airspace Opacities or Ground-Glass Opacities (GGO) are the commonly reported radiological appearances with COVID-19<sup>16,17</sup>. Bilateral, peripheral, and lower zone predominant distributions are mostly observed (90%)<sup>18</sup>. However, these manifestations are very similar to various viral pneumoniae and other inflammatory and infectious lung diseases. Hence, it is difficult for radiologists to discriminate COVID-19 from other types of pneumoniae<sup>19</sup>. Expert radiologists are needed to achieve high diagnostic performance, and the diagnosis duration required is relatively high.

Artificial Intelligence (AI) can play one of the potential roles in strengthening the power of imaging tools for providing an accurate diagnosis. Many AI applications have focused on infection quantification and identification in order to assist radiologists in decision making. The classification of COVID-19 and other types of pneumonia has been investigated using deep learning techniques<sup>6,20</sup>. However, due to the "black box" nature, the reasoning of such techniques is often unknown; hence these techniques are having low reliability to be integrated within the clinical workflow. Interpretability techniques, showing the focus area of such deep learning methods, are potentially needed to build the confidence of medical practitioners in such methods. Thereby, in this work, the authors have considered the state-of-the-art deep learning models to classify COVID-19 and similar pathology along with a thorough look into the interpretability of each of these models. Foremost, motivated by the fact that one patient can have multiple pathologies at the same time, a multi-label classification was performed. The motivation behind considering deep learning and not the interpretable non-deep-learning techniques is mainly due to the fact that in recent times deep learning techniques have been observed outperforming the others for various radiological applications<sup>21-23</sup>.

The remaining of the paper is organised as follows: in the second section, some of the related works are reported and discussed, then in the third, the different network models and interpretability techniques used here, and the strategy to create the dataset are exposed. The fourth section illustrates the classification results and the interpretability analysis. The results are analysed in the fifth section, and finally, the sixth section concludes the work and provides directions for further research.

## Related works

The utilisation of Artificial intelligence (AI) in healthcare has been developed increasingly to support human in decision-making<sup>24-27</sup>. AI-based knowledge have been combined with medical imaging to improve the diagnosis of various diseases, such as respiratory infectious diseases<sup>28</sup>, pulmonary tuberculosis<sup>29</sup>, including pandemic diseases such as H1N1 influenza<sup>30</sup>.

The spread of COVID-19 has attracted many researchers to concentrate their efforts towards developing AI-based disease-detection techniques for various medical imaging modalities. The assistance of deep learning has shown an improvement in binary diagnosis (presence or absence of COVID-19) from CXR images<sup>31</sup> and a reduction of the workload of the front-line radiologists<sup>32</sup>. Many efforts have been made to perform multi-class classification (COVID-19, other types of pneumonia or healthy) to assist radiologists in decision-making. Narin et al.<sup>7</sup> used ResNet50, InceptionV3 and InceptionResNetV2 models to classify COVID-19 patients using CXR images. They showed that the pre-trained ResNet50 model yields the highest accuracy (98%). However, accuracy is considered to be a misleading metric in the case of imbalanced datasets. Moreover, they only discriminated between healthy and COVID-19 subjects but did not include the other types of pneumonia. Wang et al.<sup>33</sup> designed the COVID-Net using CXR images for the classification of patients with bacterial pneumonia, viral pneumonia, COVID-19, and also healthy subjects with a sensitivity of 91% COVID-19 detection. Zhang et al.<sup>6</sup> used a ResNet-based model to classify COVID-19 and non-COVID-19 patients. They achieved a sensitivity of 96% and a specificity of 70.7%. Ghoshal et al.<sup>34</sup> presented a Dropweights-based Bayesian Convolutional Neural Network (BCNN) for CXR-based COVID-19 diagnosis. They found a drastic correlation between the accuracy of prediction and model uncertainty. The awareness of diagnosis decision uncertainty could endorse deep learning based applications to be used more and more in clinical routine.

Although AI-based assistance has been introduced in the field of radiology for a long time, the decision-making process of these "black box" methods remains questionable. Recently, the research on interpretability has gained more focus. Different interpretability techniques, such as occlusion<sup>35</sup>, saliency<sup>36</sup>, guided backpropagation<sup>37</sup>, integrated gradients<sup>38</sup>, etc. have been proposed which have demonstrated to potential of opening these black boxes.

## Materials and methods

### Network models

During the course of this research, various network architectures were explored and experimented with, including several variants of VGG<sup>39</sup>, ResNet<sup>40</sup>, ResNeXt<sup>41</sup>, WideResNet<sup>42</sup>, Inception<sup>43</sup>, DenseNet<sup>44</sup>. Prior to training on the dataset of this research work, all the networks were initialised with weights pre-trained on ImageNet. After observing the results, five network architectures were shortlisted for further analysis and were also used to create an Ensemble for better prediction performance. The models were selected based on different criteria, such as performance, the complexity of the model, etc. The selected models are discussed in this section, and Table 1 shows the complexity of the models.



**ResNet:** At the nascent stage of deep learning, the deeper networks faced the problem of vanishing gradients/ exploding gradients<sup>45,46</sup>, which hampered the convergence. The deeper network faced another obstacle called degradation, where the accuracy starts saturating and degrading rapidly after a certain network depth. To overcome these problems, He et al.<sup>40</sup> designed a new network model called residual network or ResNet, where the authors came up with 'Skip Connection' identity mapping. This does not involve adding an extra hyper-parameter or learnable parameter but just adding the output of the previous layer to the following layer. It unleashed the possibility of training deeper models without encountering the aforementioned problems.

After comparing against various versions of Resnet, two different variants, ResNet18 and ResNet34, were chosen for further analysis during this research.

**InceptionNet:** An image can have thousands of salient features. In different images, the focused features can be at any different part of the image, making the choice of the right kernel size for a convolution network a very difficult task. A large kernel will have more focus on globally distributed information, while a smaller kernel will have a focus on local information. To overcome this problem, Szegedy et al.<sup>43</sup> came up with a new network architecture called InceptionNet or GoogleNet. The authors used filters of multiple sizes to operate on the same level, which makes the network more "wider" rather than "deeper". To make it computationally more cost-effective, the authors limited the number of input channels by adding an extra 1x1 convolution before the 3x3 and 5x5 convolutions. Adding 1x1 convolutions is much cheaper than adding 5x5 convolutions. The authors introduced two auxiliary classifiers to prevent the problem of vanishing gradient, and an auxiliary loss is calculated on each of them. The total loss function is a weighted sum of the auxiliary loss and the real loss.

Too much reduction of dimensions can cause a loss of information, also known as "representational bottleneck". To overcome this problem and to scale up the network in ways that utilises the added computation as efficiently as possible, the authors of InceptionNet introduced a new idea in another publication of Szegedy et al.<sup>47</sup> factorising convolutions and aggressive regularisation. The authors factorised each 5x5 convolution into two 3x3 convolution operations to improve computational speed. Furthermore, they factorised convolutions of filter size  $n \times n$  to a combination of  $1 \times n$  and  $n \times 1$  convolutions. This network is known as InceptionV2.

Szegedy et al.<sup>47</sup> have also proposed InceptionV3, which extends InceptionV2 further by factorising 7x7 convolutions, label smoothing, and by adding BatchNorm in the auxiliary classifiers. Label smoothing is a type of regularising component added to the loss formula that prevents the network from becoming too confident about a class.

InceptionV3 ranked in one of the top-5 positions during the initial trials and therefore was used for further analysis.

**InceptionResNetV2:** The different variants of InceptionNet and ResNet have shown very good performance with relatively low computational costs. With the hypothesis that residual connections would cause the training of Inception networks to accelerate significantly, the authors of the original InceptionNet proposed InceptionResNet<sup>48</sup>. In this, the pooling operation inside the main inception modules was replaced by the residual connections. Each Inception block is followed by a filter expansion layer (1x1 convolution without activation) which is used for scaling up the dimensions of the filters back before the residual addition, to match the input size.

This is one of the networks that has been used in this research, because of its performance on the dataset that has been used.

**DenseNet:** Huang et al.<sup>44</sup> came up with a very simple architecture to ensure maximum information flow between layers in the network. By matching feature map size throughout the network, they connected all the layers directly to all of their subsequent layers - a densely connected neural network, or simply known as DenseNet. DenseNet improved the information flow between layers by proposing this different connectivity pattern. Unlike many other networks like ResNet, DenseNets do not sum the output feature maps of the layer with the incoming feature maps but concatenates them.

During the initial trials of this work, DenseNet161 came up as a winner in terms of performance. So, in this research DenseNet161 was included.

**Table 1.** Number of trainable parameters in each model

<i>Model</i>	<i>No of parameters</i>
<b>ResNet18</b>	11,183,694
<b>ResNet34</b>	21,291,854
<b>InceptionV3</b>	24,382,716
<b>DenseNet161</b>	26,502,926
<b>InceptionResNetV2</b>	54,327,982

## Interpretability techniques

Interpretability techniques can help understand the reasoning of a network for its predictions. In general, the interpretability results can be visualised using heatmaps, where higher values imply higher focus, which However, this can be different for many interpretability techniques. Typically, the heatmaps are overlaid on top of an input image to understand at which parts of the image the network focused to generate the predictions. The techniques using a single image at a time for the analysis are known as local interpretability techniques. While on the other hand, a global interpretability technique often pertains to comprehending how the model works - an aggregated behaviour of the model based on the distribution of the data<sup>49,50</sup>. There are various techniques already in existence. Some of the methods, such as, Occlusion, Saliency, Input X Gradient, Integrated Gradients, Guided Backpropagation, DeepLIFT, Neuron Activation Profiles, which were explored in this research, are explained briefly in this section.

**Occlusion:** Occlusion is one of the simplest interpretability techniques for image classifications. This technique helps to understand which features of the image steer the network towards a particular prediction or which are the most important parts for the network to classify a certain image. To get this answer, Zeiler et al.<sup>35</sup> performed an occlusion technique by systematically blocking different portions of the input image with a grey square box and monitoring the output of the classifier. The grey square is applied to the image in a sliding window manner that moves across the image, obtaining many images, and then they are fed into the trained network to obtain probability scores for a given class for each mask position.

**Saliency:** In the context of visualisation, saliency refers to a topological representation of the unique features of an image. Saliency is one of the baseline approaches for the interpretation of deep learning models. The saliency method of Simonyan et al.<sup>36</sup> returns the gradients of a model for its respective inputs. The positive values present in the gradients show how a small change in the input image changes the prediction.

**Input X Gradient:** Input X Gradient is an extension of the Saliency approach. Similar to the saliency method of Simonyan et al.<sup>36</sup>, this method of Kindermans et al.<sup>51</sup> also takes the gradients of the output with respect to the input, but additionally, multiplies the gradients by the input feature values.

**Guided Backpropagation:** Guided Backpropagation, also known as guided saliency, is another visualisation technique for deep learning classifiers. Guided backpropagation is a combination of vanilla backpropagation and deconvolution networks (DeConvNet)<sup>37</sup>. In this method, only the positive error signals get backpropagated, and the negative signals are set to zero while backpropagating through a ReLU unit<sup>52</sup>.

**Integrated Gradients:** Sundararajan et al.<sup>38</sup> proposed a model interpretability technique, which assigns an importance score to each of the features of the input by approximating the integral of gradients of the output for that input, along the path from the given references for the input.

**DeepLIFT:** Deep Learning Important FeaTures or DeepLIFT, proposed by Shrikumar et al.<sup>53</sup>, is a method for pixel-wise decomposing the output prediction of a neural network on a specific input. This is done by backpropagating the contributions of all neurons in the network to every feature of the input. DeepLIFT compares the activation of each neuron to its 'reference activation', and then assigns contribution scores based on the difference. DeepLIFT can also reveal dependencies that might be missed by other approaches by optionally assigning separate considerations to positive and negative contributions. Unlike other gradient-based methods, it uses difference from reference, which permits DeepLIFT to propagate an importance signal even in situations where the gradient is set to zero.

**Neuron Activation Profiles:** The above-described interpretability techniques are local methods that help understand single predictions of a neural network. To investigate the model behaviour more generally, a global interpretability technique called Neuron Activation Profiles (NAPs) is employed<sup>54,55</sup>. NAPs describe and contrast neural network activity of sets of related inputs, for example, of different classes, using an averaging approach. First, the activation values in the layers of interest are obtained by computing a forward pass for every test image. Then, the average feature maps over each respective group are computed to characterise the group-specific activity. In addition to characterising the network activations for a group, further emphasise is given to the difference between the groups. To this end, the average over all groups is subtracted from each group's average. These normalised averaged activation values can be interpreted as the activation difference from the global average. Positive values indicate a characteristically high neuron activation in comparison to the entire data set, and negative values indicate a comparably low neuron activation. NAP values are particularly useful to identify which activations differ between groups of interest and correspondingly indicate how well a model is able to distinguish between the classes according to the activations. While working with image data, visually interpretable plots of NAPs of feature maps can be created. For data which are not visually interpretable, NAPs can be further used for similarity analyses<sup>55</sup> or for dimensionality reduction-based visualisation<sup>56</sup>.

In order to obtain useful averaging results, this method requires data in which the objects are at the same location in the images. This alignment is guaranteed through data pre-processing that resizes and crops the original images.

## Implementation

The models were implemented using PyTorch<sup>57</sup>. An interpretability pipeline for PyTorch-based classification models was developed with the help of Captum<sup>58</sup>. The code of this project is available on GitHub: <https://github.com/soumickmj/diagnoPP>. The pipeline has later made part of the TorchEsegeta<sup>59</sup>.

Trainings were performed using Nvidia GeForce 1080 Ti and 2080 Ti GPUs, having 11GB of memory each. The loss was calculated using Binary Cross-Entropy (BCE) with Logits, which combines the Sigmoid layer with the BCE loss, to achieve better numerical stability than using the Sigmoid layer followed by BCE loss separately. The numerical stability is achieved by using the log-sum-exp trick, which can prevent underflow/overflow errors. The loss was minimised by optimising the model parameters using the Adam optimiser<sup>60</sup>, with a learning rate of 0.001 and a weight decay of 0.0001. A manual seed was used to ensure reproducibility<sup>61</sup> of the models. Automatic Mixed Precision was used using Apex<sup>62</sup>, to speed-up the training and to decrease the GPU memory requirements.

The interpretability methods were applied on the models using Nvidia Tesla V100 GPUs, having 32GB memory each. Some of the interpretability techniques could not be used on certain models due to the lack of GPU memory caused by the complexities of the models.

## Data

### Data Collection

The CXR images were collected from two public datasets. The first dataset was the COVID-19 image data collection by Cohen et al.<sup>20,63</sup>, consisting of 236 images of COVID-19, 12 images of COVID-19 and ARDS, 4 images of ARDS, 1 image of Chlamydomphila, 1 image of Klebsiella, 2 images of Legionella, 12 images of Pneumocystis, 16 images of SARS, 13 images of Streptococcus and 5 images without any pathological findings. The second dataset was the Chest X-Ray Images (Pneumonia) dataset by Kermany et al.<sup>64,65</sup>, which has a total of 1583 images of healthy subjects, 1493 images of viral pneumonia and 2780 of bacterial pneumonia. From this dataset, 500 images of healthy, 250 images of viral pneumonia and 250 images of bacterial pneumonia, were randomly chosen. Fig 1 portrays the final data distribution considered for the work. This dataset of CXR images consists of posterior-anterior (PA), anterior-superior (AP), and anterior-superior supine (AP supine) radiographs. Although AP view is not the priority positioning and has disadvantages such as overlapping of organs which might interfere with the network prediction<sup>66</sup>, it is a technique commonly used for COVID-19 patients who are in a coma.

The hierarchical nature of pathologies can be observed in this combined dataset (see Fig 2). For example, SARS and COVID-19 are sub-types of viral pneumonia. On the other hand, Streptococcus, Klebsiella, Chlamydomphila, and Legionella are sub-types of bacterial pneumonia, and Pneumocystis is a sub-type of fungal pneumonia. Furthermore, viral, bacterial, and fungal pneumoniae are different types of pneumonia. Therefore, a patient having COVID-19 is inherently having viral pneumonia. ARDS, which stands for acute respiratory distress syndrome, is a serious lung condition with a high mortality rate<sup>67</sup>. It is commonly developed with pathological conditions such as non-pulmonary sepsis, aspiration, or pneumonia<sup>68</sup>. Although the respiratory pathologies of ARDS (associated with or without COVID-19) and COVID-19 are similar, COVID-19 has different features that require different patient management, and a patient suffering from both might require additional care<sup>69-71</sup>. Therefore, the dataset, which comprises cases where a patient has both COVID-19 and ARDS, is suitable for multi-label classification.

### Dataset Preparation

The final dataset was randomly divided into a training set, consisting of 60% of the unique subjects, and the remaining 40% of the subjects were used as a test set. 5-fold cross-validation (CV) was performed to evaluate the generalisation capabilities of the models. The performance of the models during the 5-fold CV is reported in the sub-section. For interpretability analysis, only the results from the first fold were used, as it produced the best micro F1 scores.

### Pre-processing

The dataset used for the task comprises X-ray images collected at different centres using different protocols and varying in size and intensity. Therefore, all the images were initially pre-processed to have the same size. To make the image size uniform throughout the dataset, each of the images was interpolated using bicubic interpolation, to have 512 pixels on the longer side. The number of pixels on the shorter side was calculated, preserving the aspect ratio of the original image. After that, zero-padding was used on the shorter side to make that side have 512 pixels, resulting in a 512 x 512 image. Image resizing was followed by percentile cropping, where the image intensity was cropped to the 1st and 95th percentile, and then intensity normalisation to the interval [0,1] was performed. The percentile cropping normalisation minimises the effect of intensity variation due to non-biological factors.

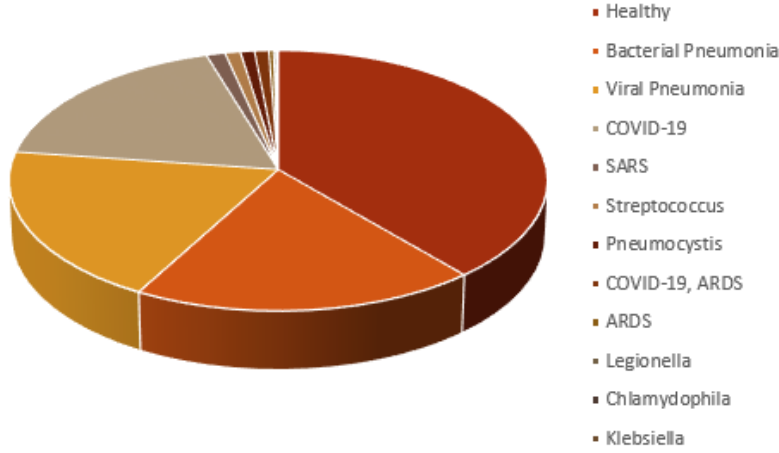


**Figure 1.** CXR images distribution for each infection type in the dataset

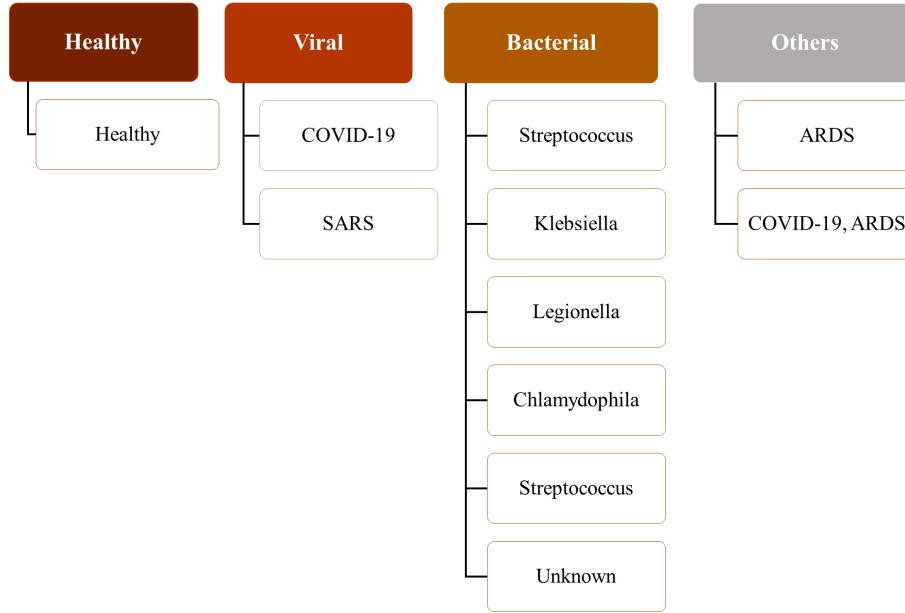


**Figure 2.** A hierarchy of pathological labels used in this study

### Classification Setup

In this multi-label classification setup, the model was trained to predict the disease and also its super-types. Hence, when a network encounters an image of a COVID-19 patient, it should ideally predict it as pneumonia, viral pneumonia, and COVID-19. When a network encounters an image of a patient having multiple pathologies, like in this dataset, some patients have both COVID-19 and ARDS, ideally the network should predict it as pneumonia, viral pneumonia, COVID-19, as well as ARDS. Interpretability analysis was performed for each label of each image in the test set.

### Evaluation Metrics

In a multi-class setting, classifiers are generally evaluated with respect to precision, recall, and F1 metrics. In a multi-label classification setting, the same metrics are calculated in two ways: macro and micro averaging<sup>72</sup>.

$$Macro = \frac{1}{P} \sum_{i=1}^P Metric \left( TP_i, FP_i, TN_i, FN_i \right) \quad (1)$$

As shown in Eq 1, the macro-based metrics are first computed individually from the true positives (TP), true negatives (TN), false positives (FP) and false negatives (FN) of each class/pathology and then averaged, where  $P$  denotes the number of classes and  $Metric \in \{\text{precision, recall, F1}\}$ .

This manner of computation of the metrics aids in treating each pathology equally, and the metric values get heavily influenced by the rare labels.

$$Micro = Metric(\sum_{i=1}^P TP_i, \sum_{i=1}^P FP_i, \sum_{i=1}^P TN_i, \sum_{i=1}^P FN_i) \quad (2)$$

In micro-based metrics, TP, TN, FP, and FN of each class/pathology are added individually and then averaged, as shown in Eq 2. Therefore, the micro-based metrics portray the aggregated contribution of all classes/pathologies. Therefore, the influence of the predictions out of the minority classes gets diluted among the contributions from the majority classes. This makes the micro-based metrics an appropriate measure to estimate the overall performance of the classifier, especially in the case of imbalanced datasets. Since the dataset used was highly imbalanced, micro-based metrics have been considered for the evaluation of the classifiers<sup>73</sup>.

## Results

### Model outcome

#### Overall comparisons of the classifiers

Fig 3a portrays that the overall performance of the classifiers over pathologies was similar. Among the non-Ensemble models, DenseNet161 performed the best concerning all metrics. Although InceptionResNetV2 was the most complex model among all, it produced the worst recall, which implies the ability of the model to find the pathology-affected cases was poor compared to the less complex models. ResNet18 was the least complex model among the non-Ensemble classifiers, and it ranked second after DenseNet161 with respect to micro F1. The Ensemble produced the best results and minimum variance as portrayed in Table 2 over the 5-fold cross-validation.

**Table 2.** Performance of all the classifiers with respect to micro based metrics over 5-folds

<i>Model</i>	<i>Precision</i>	<i>Recall</i>	<i>F1</i>
<b>DenseNet161</b>	0.864 ± 0.012	0.845 ± 0.015	0.854 ± 0.008
<b>InceptionResNetV2</b>	0.844 ± 0.023	0.787 ± 0.063	0.814 ± 0.042
<b>InceptionV3</b>	0.802 ± 0.065	0.792 ± 0.044	0.796 ± 0.053
<b>ResNet18</b>	0.824 ± 0.014	0.824 ± 0.008	0.824 ± 0.007
<b>ResNet34</b>	0.815 ± 0.022	0.800 ± 0.025	0.807 ± 0.018
<b>Ensemble</b>	0.889 ± 0.010	0.851 ± 0.005	0.869 ± 0.007

Another interesting observation that could be made is regarding inactive feature maps (dead neurons). DenseNet161 had the highest percentage of such feature maps - as high as 99.22% for the middle layer. Even though InceptionResNetV2 was the most complex, it had fewer inactive feature maps than the DenseNet161. ResNets, the lesser complex models in this study, had the lower percentage of inactive feature maps (48.44% and 60.16% for the middle layers of ResNet18 and ResNet34, respectively).

#### Comparisons of the classifiers for different pathologies

The authors have also compared the classifiers' performance at the pathology level. The average metric values across 5 cross-validation folds have been depicted in Fig 3b to Fig 3f for COVID-19, pneumonia, viral pneumonia, bacterial pneumonia and healthy subjects respectively. While comparing the models using average F1, it has been observed that the performance of most of the models for COVID-19, pneumonia, and healthy was good, except for the performance of the InceptionResNetV2 for COVID-19 cases. Among all the models, the results of DenseNet161 were the most promising ones for all the diseases. For the COVID-19 classification, DenseNet161 performed the best, and ResNet18 bagged the second position. DenseNet161 performed the best for pneumonia. InceptionResNetV2 provided the highest performance for viral pneumonia classification. Lastly, InceptionV3 gave the highest scores for bacterial pneumonia.

### Interpretability of models

In the first sub-subsection different interpretability techniques have been explored for different classifiers with respect to the different diseases. The second sub-section talks about how the different models performed for specific pathologies.



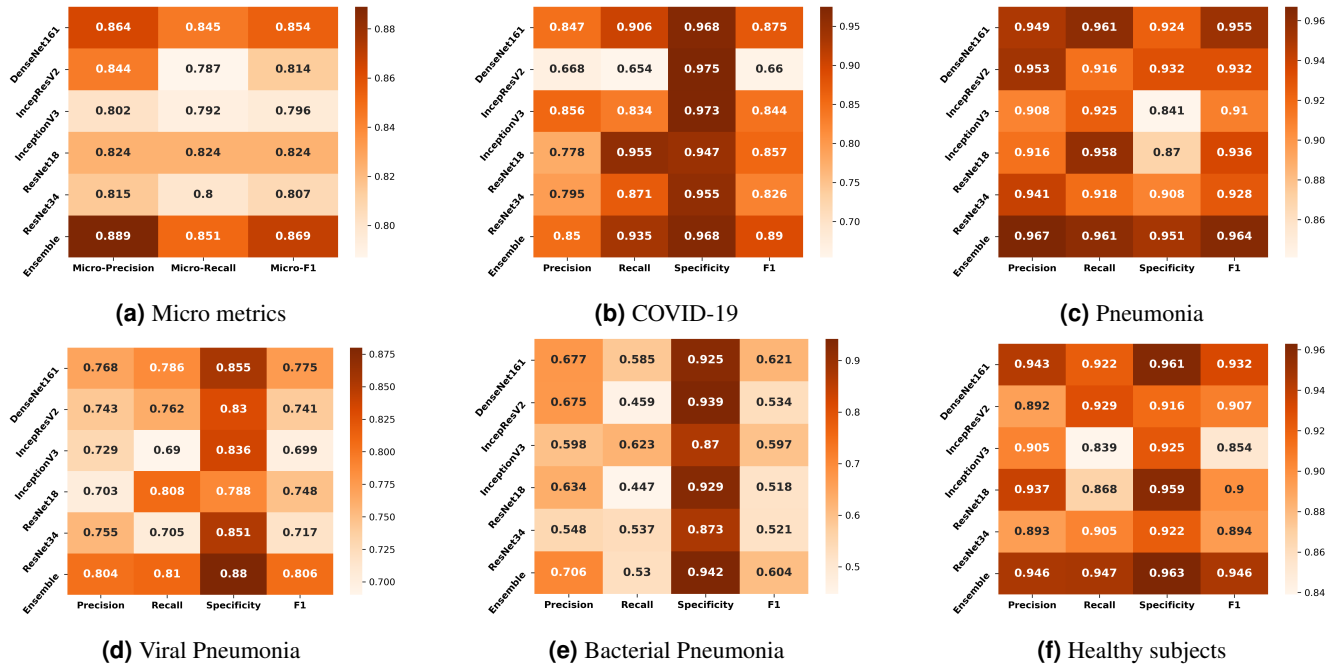


**Figure 3.** Comparison of the classifiers based on micro metrics (a) and their performance for the different classes (b-f)

All the given interpretability analyses (except using the global method NAP), were performed for that specific input CXR image which has been shown as the underlay. For the interpretability analysis using NAP, all the images from the test set were used, as this method performs a global analysis.

#### **Pathology based comparisons of local interpretability techniques for the models**

To visualise the results on specific case, the models were interpreted using local methods - occlusion, saliency, inputXgradient, guided backpropagation and integrated gradients, and have been shown in Fig 7, Fig 8 and Fig 9. Apart from occlusion, the other interpretability techniques failed to run for DenseNet161 due to GPU memory limitations. For DeepLIFT, ResNets encountered an additional problem because of the in-place ReLU operations used in those models. The models have to be updated to be able to run DeepLIFT on them.

According to the clinical findings of the COVID-19 image data provided by Cohen et al.<sup>20</sup>, multiple abnormalities of the lungs were located on the right upper and lower pulmonary field, as well as the upper left part of the lung. The models predicted this case as COVID-19, pneumonia, and viral pneumonia responding to the pathology of lung infection. One can see that the models' focus area for COVID-19 differs from the focus area for pneumonia and viral pneumonia. DenseNet161 and InceptionResNetV2 emphasised mostly on the right lung. InceptionV3, ResNet18, and ResNet34 covered both the right and left parts, not only the lesion but also the irrelevant regions out of the lung.

The local interpretability methods primarily suffered from false positives. In some cases occlusion did not detect the affected areas for DenseNet161 and InceptionResNetV2, and falsely marked the normal areas as positive, as shown in Fig 7. Further, for InceptionV3, it detected some positive patches but falsely detected more areas as positive. Finally, in general, for ResNets, occlusion was most sensitive to the positive areas and detected lesser false negatives. Guided backpropagation, saliency, integrated gradients, and DeepLIFT in general falsely detected normal lung areas as positive - picked up normal bronchovascular markings as positive and did not mark the actual affected areas. Input X gradient detected some positive areas correctly for ResNet18, but falsely marked many normal areas. In general, the representations learned by the ResNet models captured the most accurate regions as seen from most interpretability techniques, with fewer false negatives. Among the local interpretability techniques, occlusion provided the best guidance in finding clinically important areas, which were confirmed by medical experts.

#### **Intense Interpretability**

**The failure case of the best performing model for COVID-19 classification:** Even though the DenseNet161 performed the best among all the models, it gave false negatives for some of the COVID-19 patients, whereas the rest of the models, including the Ensemble, could correctly predict. The occlusion results of the models can be observed in Fig 4. This figure shows that DenseNet161 and InceptionResnetV2 did not focus on any affected areas, but rather on other regions (e.g. normal right hilum).

InceptionV3, ResNet18, and ResNet34 mostly focused on the affected areas with good sensitivity. InceptionV3, however, had more false positives than the ResNets (e.g. outside the right lung).

Another analysis was performed with the CXRs of a 70-year-old woman who had three days of cough, myalgias, and fever; without any recent overseas travel. A series of chest X-ray images were obtained before the confirmation of coronavirus infection, and the follow-ups were done in three days, seven days, and nine days. It shows the progression of radiographic changes. In the image prior to COVID-19, all normal areas were falsely detected by both models as relevant features. In the image of day 3, the doctor could not visually detect any affected area, even though this was the image from the third day after testing positive for COVID-19. This might indicate that when no substantial affected area can be seen in the image visually (i.e. day 3), the model might have been picking up some mild markers, which visually cannot be confirmed. In the images of days seven and nine, DenseNet161 did not focus correctly on the affected regions and had both false positives and false negatives, while ResNet18 focused on the affected regions more accurately.

ResNet18 can be considered the overall winner, as it yielded high evaluation scores, despite having the least number of network parameters. Further, its interpretability analysis showed the location of the lesion, which makes it possible to utilise this network for follow-up or severity estimations as illustrated in Fig 5.

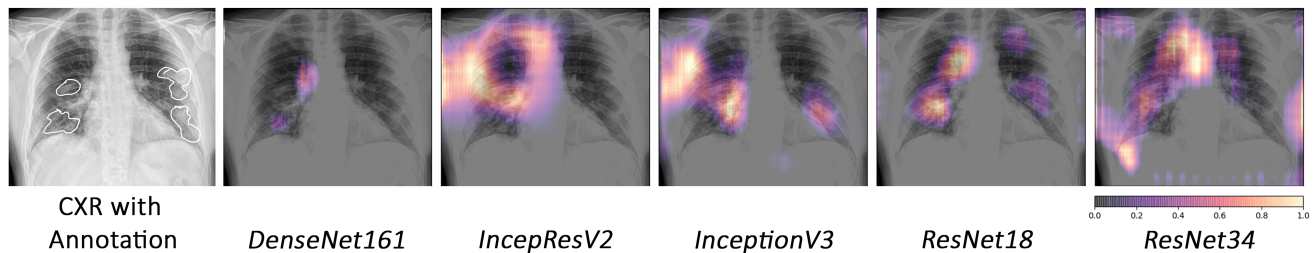


**Figure 4.** A case-study of DenseNet161 failure using occlusion. The affected areas in the lungs have been annotated by medical experts.

**Representations in DenseNet161 and ResNet18:** In addition to the individual failure cases, the authors further investigated how the COVID-19 and Pneumonia pathologies are represented in the neuron activations of DenseNet161 and ResNet18 in comparison to healthy individuals. This representation analysis was performed using NAPs - a global interpretability technique. In general, in a well-generalised model, larger neuron activation differences are expected between the different pathologies and healthy subjects in the lungs than in other image areas. If activity differences are observed in other regions, this indicates that the model exploits biologically irrelevant features to discriminate the classes.

To find potentially exploitable features, first the input averages are investigated (input layer NAPs) in Fig 6 (left). It can be observed that Pneumonia images cover a smaller portion of the height dimension than images of COVID-19 or healthy subjects. This means that there are dark top and bottom regions in the majority of Pneumonia images. Based on this observation, the authors hypothesise that a model might exploit this non-biological feature.

To investigate this hypothesis, the feature map NAPs of DenseNet161 and ResNet18 in an early and deep layer, respectively, are visualised. The authors particularly investigate layers at representative depths of the networks. For DenseNet161, the ReLU-activated outputs of the first and last Dense Blocks were chosen. As representative layers of ResNet18, the outputs after the first and last residual connection were selected. For these layers, two exemplary feature map NAPs among those of the highest activity differences between the observed classes are shown in Fig 6. In DenseNet161, one can clearly observe activation differences both in the border regions and the lung. For example, COVID-19 images are easy for the model to distinguish based on the activation difference corresponding to not having dark regions at the bottom and top of the images. In the deeper layer, the activation difference patterns do not resemble any interpretable structure, neither at the lungs nor at the bottom and top regions. This indicates why DenseNet161 has a high performance despite giving false negative COVID-19 results. Instead of detecting the COVID-19-specific features, it likely exploits features of the data which are correlated but unrelated to the pathology. However, it does not appear as if DenseNet161 uses dark border regions as the main distinguishing factor. ResNet18, in contrast, is less likely to pick up biologically irrelevant features. While in early layers, there are activation differences in the top and bottom area of the images, in most deep-layer feature maps, the groups can most clearly be distinguished from each other from neuron activity in the (right) lung regions.

**COVID-19, pneumonia and viral pneumonia:** Based on the fact that COVID-19 is a subset of viral pneumonia, the focus of this section is centralised on the interpretability comparison of the models for these three pathologies. The interpretability techniques reported that different networks focused on different areas for the same CXR image for predicting each of the diseases. It was observed that the focus area of DenseNet161 for COVID-19 was explicitly different from the one for pneumonia

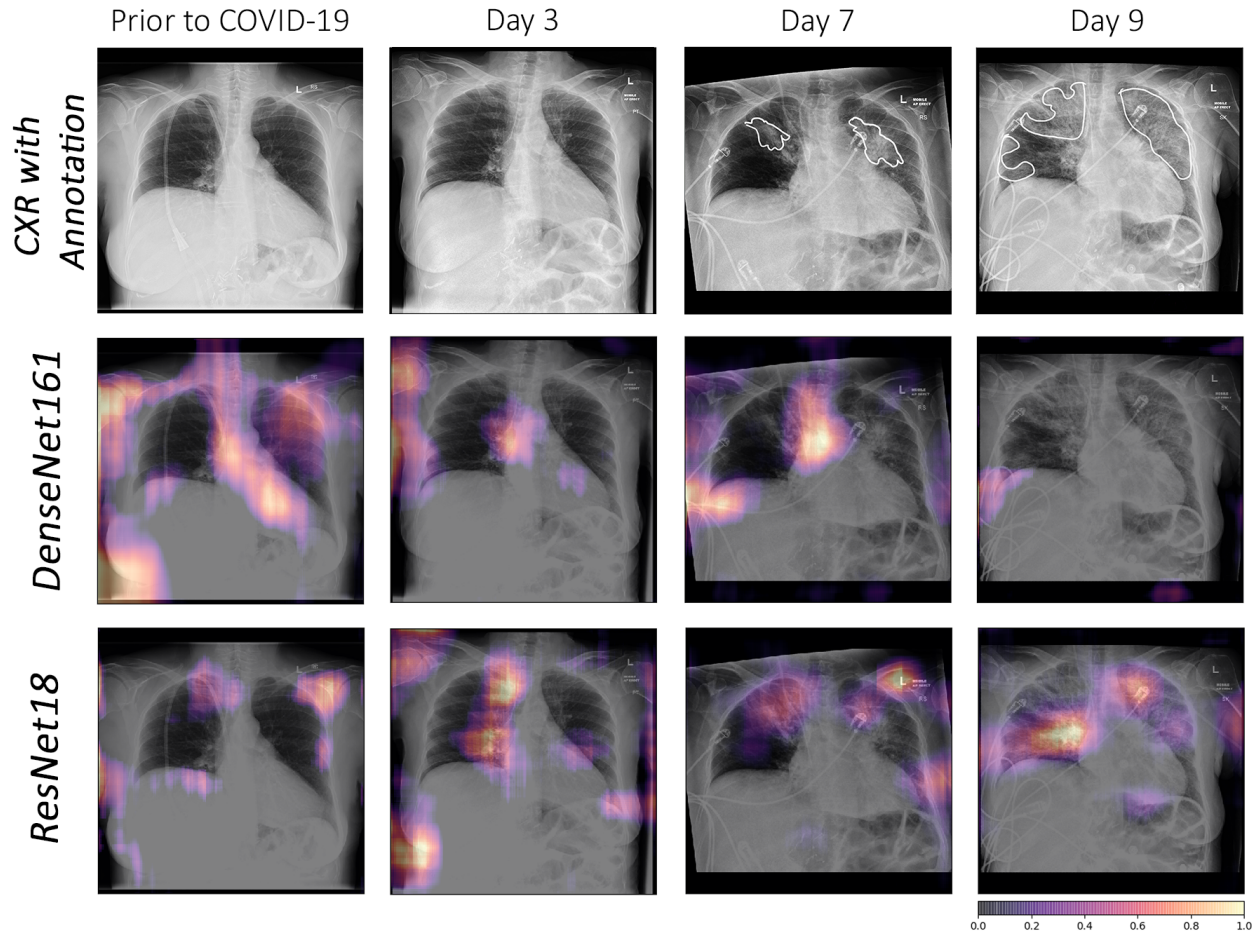


**Figure 5.** Comparison using occlusion between DenseNet161 and ResNet18 for a specific COVID-19 follow-up case. The affected areas in the lungs have been annotated by medical experts.

and viral pneumonia. However, InceptionResNetV2 and InceptionV3 emphasised a similar area (different focus areas for each model) for all three pathologies. Furthermore, ResNet18 and ResNet34 targeted the lung region for COVID-19 and viral pneumonia but differed for pneumonia. Fig 10 exhibits the mentioned findings.

## Discussion

The literature review portrayed that the diagnosis of COVID-19 was seen as a multi-class classification task rather than a multi-label classification. The datasets used in the previous works vary in terms of the amount of data used for the classification task.<sup>7</sup> created a balanced dataset by appending the 50 COVID cases with 50 healthy cases from another dataset and reported the highest mean specificity score of 0.90 using InceptionV3. The others<sup>6,8,33</sup> performed a multi-class classification task on different imbalanced datasets using X-rays, and achieved the maximum mean specificity of 0.989, 0.979, 0.971 respectively. In this work, InceptionResNetV2 achieved the highest specificity of 0.975, comparable to the previous works. However, in this research, the authors have used a different dataset, train-test split, and pre-processing techniques compared to the previous works, which makes it unfair to compare the results with the previous works.

It was observed the less complex models were more interpretable while having lesser dead neurons than the more complex ones. DenseNet161, which resulted in the highest F1-score, had the most number of dead neurons and also had the worst focus areas according to the interpretability methods. The model which resulted in the second-best F1-score, ResNet18, was the least complex model in this study - while also having the best focus areas as dictated by the interpretability methods. This was further confirmed by a global interpretability method, the NAPs, which showed that the ResNet18 is less likely to pick up biologically irrelevant features. It is noteworthy that in some cases, the network predicted the findings as a presence of COVID-19, while the doctors did not report any abnormalities.

There were a couple of cases where the network detected both viral and bacterial pneumonia. According to Morris et al.<sup>74</sup>,

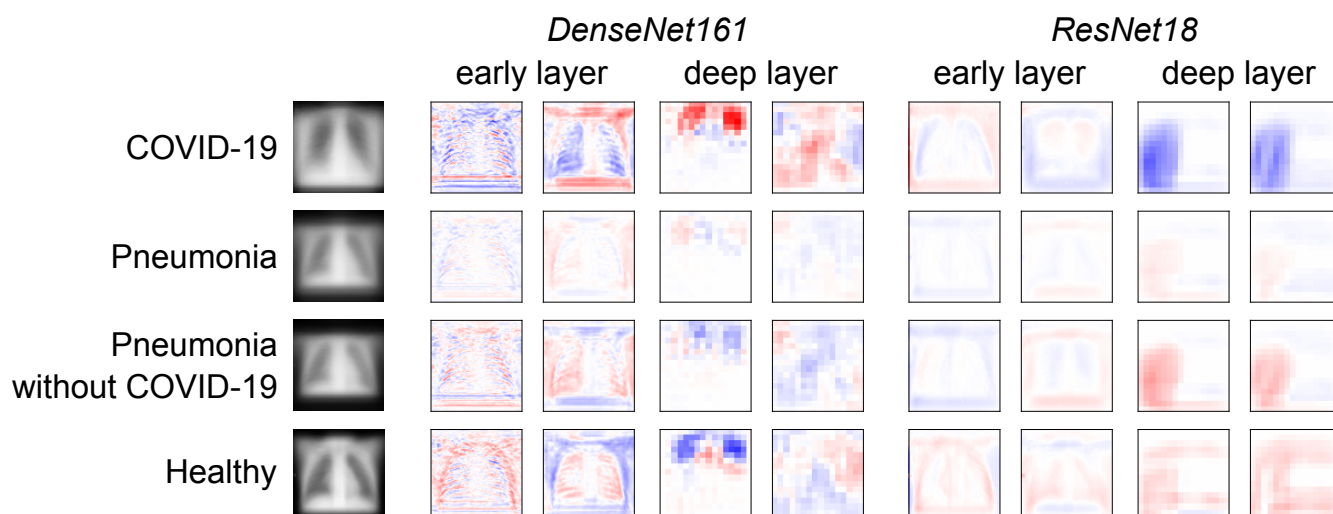


**Figure 6.** Average input images and feature map NAPs in different models and layers for different pathologies and healthy subjects. Blue indicates lower activation of the respective neuron for this group compared to the other groups, red indicates higher activity.

and Shigeo et al.<sup>75</sup>, the induction of viral infection could lead to secondary bacterial infection and increase the severity of the symptoms. Though such cases were considered as miss-predictions for the current dataset based on the available labels, one could argue that the network was able to detect such instances.

The main motivation to perform a multi-label classification over a multi-class classification was to be able to predict multiple pathologies from the images if they were present. It was observed that all the networks, including the Ensemble, were able to correctly predict both COVID-19 and ARDS for the images which had both pathologies present.

Lastly, this study also showed that the models could classify the lung pathologies from CXR images, although undesired objects, such as annotations or labels, were obscuring the radiographs.

## Conclusion and future works

In this paper, various deep learning based classifiers for multi-label classification of COVID-19 and similar pathologies in CXR images have been compared, and the interpretability of those models has been investigated and finally verified by medical professionals. In general, most of the models performed well. But, some of the models failed to perform certain tasks. The authors have also created an Ensemble, which helped to fill in those shortcomings of the models by combining their predictions. Moreover, it was observed that the smallest model, ResNet18 competed well against considerably larger models. In fact, for certain situations, it performed better than the largest model in the mix, InceptionResNetV2. For patients who had more than one pathology, this multi-label classification setup was able to correctly predict all of those pathologies. DenseNet161 was the best performing model in this setup in terms of classification scores, though it was observed that the focus of the network was many times on unrelated biologically irrelevant regions. After qualitative analysis of the interpretability results, it can be said that the ResNets were the most interpretable models as the focus areas of the networks were mostly on the correct regions.

Model explainability methods like LIME<sup>76</sup>, SHAP<sup>77</sup> etc., have not been explored during this research but are planned as future work. This same approach can also be tried on CT images to compare the networks' sensitivity for COVID-19 on CT and CXR images. Moreover, it would be interesting to investigate how the networks' performances are affected if completely unrelated pathologies (like tumours) are mixed with this current dataset. Prior non-image information (like the patient's prior medical history, the result of the RT-PCR test, etc.) can also be tried to be incorporated into the network models to aid the networks in decision-making. Furthermore, instead of supplying the whole image to the models, lung segmentation can be used as a pre-processing step, which might improve the networks' predictions by helping them to focus just on the region of interest, which in this case are the lungs. Training techniques like few-shot learning (including one-shot learning), semi-supervised learning, etc., can be explored for learning to classify COVID-19 cases from a small dataset. Moreover, joint segmentation-classification techniques can also be investigated for this multi-label classification problem. Several interpretation techniques are implemented in the interpretability pipeline but have not been investigated in this paper and will be explored in the future for this dataset-model setup. Finally, a large-scale study involving more medical professionals to evaluate the benefits of the interpretability methods in terms of trust-building and also their helpfulness in the clinical workflow should also



be evaluated in the future.

## Acknowledgements

This work was conducted within the context of the International Graduate School MEMoRIAL at Otto von Guericke University (OVGU) Magdeburg, Germany, kindly supported by the European Structural and Investment Funds (ESF) under the programme "Sachsen-Anhalt WISSENSCHAFT Internationalisierung" (project no. ZS/2016/08/80646) and was partly funded by the Federal Ministry of Education and Research within the Forschungscampus STIMULATE under grant number 13GW0095A.

## Author contributions statement

S.C., F.S., C.S., and S.G. created the concept and designed the study, under the supervision of G.R., S.S., O.S., and A.N. S.C., and S.G. performed the experiments. V.K. created the neuron activation profiles and analysed their results. C.S. performed the qualitative analysis of the interpretability results and created the visualisations. R.M. and N.D. reviewed the interpretability results and created the annotations. S.C., F.S., C.S., S.G., and R.K. wrote the manuscript. P.R., G.R., S.S., O.S., and A.N. reviewed and revised the manuscript.

## Data availability

The datasets generated and/or analysed during the current study are available in the **COVID-19 image data collection** repository by *Joseph Paul Cohen*, <https://github.com/ieee8023/covid-chestxray-dataset> and in the **Chest X-Ray Images (Pneumonia)** repository by *Paul Mooney*, <https://www.kaggle.com/paultimothymooney/chest-xray-pneumonia>.

## Additional information

All methods were carried out in accordance with relevant guidelines and regulations. The code of this project is publicly available on GitHub: <https://github.com/soumickmj/diagnoPP>.

## References

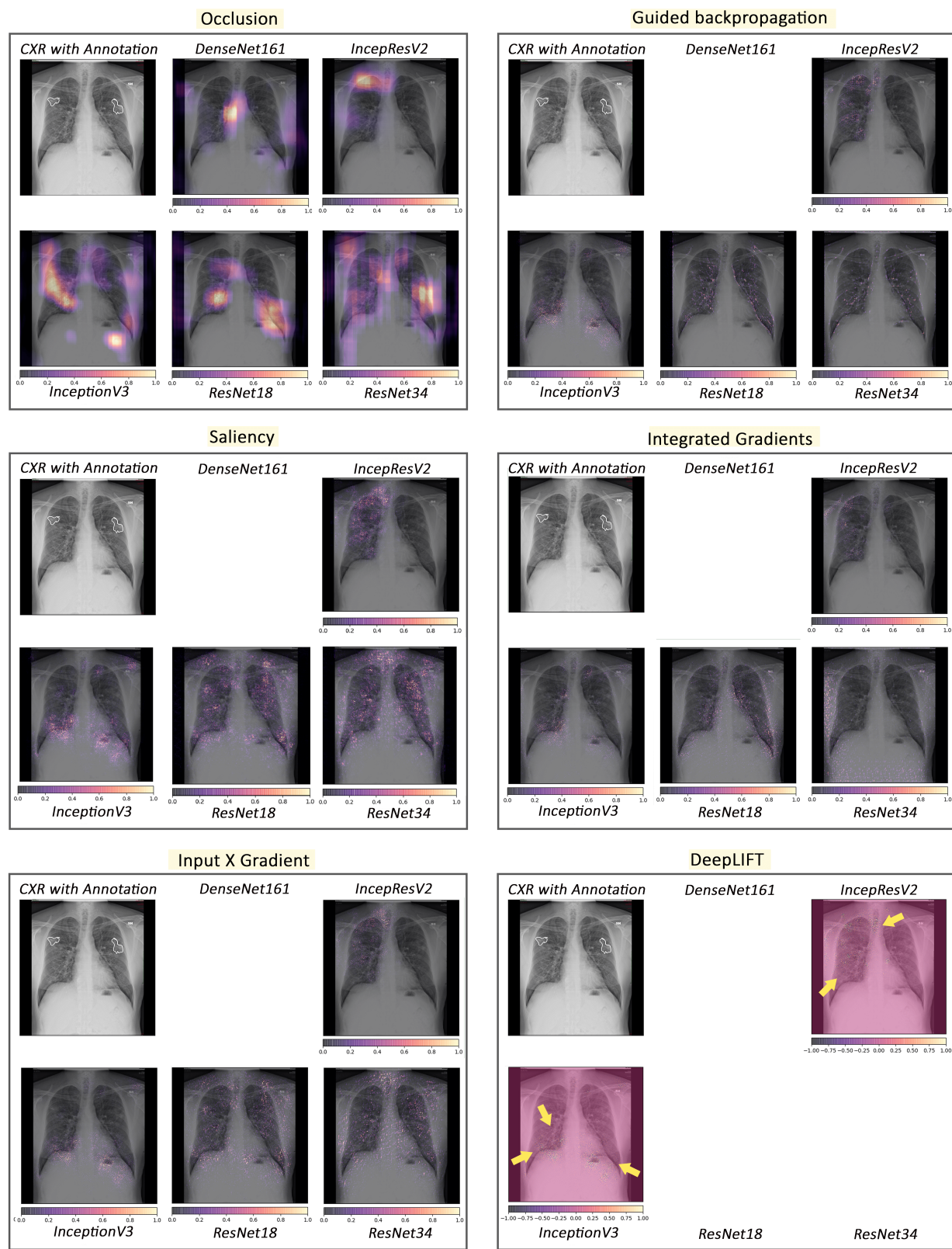
1. Zhu, N. *et al.* A novel coronavirus from patients with pneumonia in china, 2019. *New Engl. J. Medicine* (2020).
2. Li, Q. *et al.* Early transmission dynamics in wuhan, china, of novel coronavirus–infected pneumonia. *New Engl. J. Medicine* (2020).
3. Radiopaedia: Covid-19. <https://radiopaedia.org/articles/covid-19-3>. (Accessed on 31st May 2020).
4. Ai, T. *et al.* Correlation of chest ct and rt-pcr testing in coronavirus disease 2019 (covid-19) in china: a report of 1014 cases. *Radiology* 200642 (2020).
5. Fang, Y. *et al.* Sensitivity of chest ct for covid-19: comparison to rt-pcr. *Radiology* 200432 (2020).
6. Zhang, J., Xie, Y., Li, Y., Shen, C. & Xia, Y. Covid-19 screening on chest x-ray images using deep learning based anomaly detection. *arXiv preprint arXiv:2003.12338* (2020).
7. Narin, A., Kaya, C. & Pamuk, Z. Automatic detection of coronavirus disease (covid-19) using x-ray images and deep convolutional neural networks. *arXiv preprint arXiv:2003.10849* (2020).
8. Apostolopoulos, I. D. & Mpesiana, T. A. Covid-19: automatic detection from x-ray images utilizing transfer learning with convolutional neural networks. *Phys. Eng. Sci. Medicine* 1 (2020).
9. Kanne, J. P. Chest ct findings in 2019 novel coronavirus (2019-ncov) infections from wuhan, china: key points for the radiologist (2020).
10. Bernheim, A. *et al.* Chest ct findings in coronavirus disease-19 (covid-19): relationship to duration of infection. *Radiology* 200463 (2020).
11. Xie, X. *et al.* Chest ct for typical 2019-ncov pneumonia: relationship to negative rt-pcr testing. *Radiology* 200343 (2020).
12. Huang, P. *et al.* Use of chest ct in combination with negative rt-pcr assay for the 2019 novel coronavirus but high clinical suspicion. *Radiology* **295**, 22–23 (2020).
13. Omer, S. B., Malani, P. & Del Rio, C. The covid-19 pandemic in the us: a clinical update. *Jama* **323**, 1767–1768 (2020).



14. Rubin, G. D. *et al.* The role of chest imaging in patient management during the covid-19 pandemic: a multinational consensus statement from the fleischner society. *Chest* (2020).
15. Harahwa, T. A. *et al.* The optimal diagnostic methods for covid-19. *Diagnosis* **7**, 349–356 (2020).
16. Guan, W.-j. *et al.* Clinical characteristics of coronavirus disease 2019 in china. *New Engl. journal medicine* **382**, 1708–1720 (2020).
17. Durrani, M., Inam ul Haq, U. K. & Yousaf, A. Chest x-rays findings in covid 19 patients at a university teaching hospital-a descriptive study. *Pak. J. Med. Sci.* **36**, S22 (2020).
18. Wong, H. Y. F. *et al.* Frequency and distribution of chest radiographic findings in covid-19 positive patients. *Radiology* 201160 (2020).
19. Ng, M.-Y. *et al.* Imaging profile of the covid-19 infection: radiologic findings and literature review. *Radiol. Cardiothorac. Imaging* **2**, e200034 (2020).
20. Cohen, J. P., Morrison, P. & Dao, L. Covid-19 image data collection. *arXiv preprint arXiv:2003.11597* (2020).
21. Liu, J., Cao, L., Akin, O. & Tian, Y. Accurate and robust pulmonary nodule detection by 3d feature pyramid network with self-supervised feature learning. *arXiv preprint arXiv:1907.11704* (2019).
22. Yoo, S., Gujrathi, I., Haider, M. A. & Khalvati, F. prostate cancer detection using deep convolutional neural networks. *Sci. Reports* **9** (2019).
23. Tô, T. D. *et al.* *Ensembled Skin Cancer Classification (ISIC 2019 Challenge Submission)*. Ph.D. thesis, ISIC2019 (2019).
24. Vial, A. *et al.* The role of deep learning and radiomic feature extraction in cancer-specific predictive modelling: a review. *Transl Cancer Res* **7**, 803–816 (2018).
25. Davenport, T. & Kalakota, R. The potential for artificial intelligence in healthcare. *Futur. healthcare journal* **6**, 94 (2019).
26. Sloane, E. B. & Silva, R. J. Artificial intelligence in medical devices and clinical decision support systems. In *Clinical Engineering Handbook*, 556–568 (Elsevier, 2020).
27. Mahadevaiah, G. *et al.* Artificial intelligence-based clinical decision support in modern medical physics: Selection, acceptance, commissioning, and quality assurance. *Med. physics* **47**, e228–e235 (2020).
28. Agrebi, S. & Larbi, A. Use of artificial intelligence in infectious diseases. In *Artificial intelligence in precision health*, 415–438 (Elsevier, 2020).
29. Sweetlin, J. D., Nehemiah, H. K. & Kannan, A. Computer aided diagnosis of drug sensitive pulmonary tuberculosis with cavities, consolidations and nodular manifestations on lung ct images. *Int. J. Bio-Inspired Comput.* **13**, 71–85 (2019).
30. Yao, J., Dwyer, A., Summers, R. M. & Mollura, D. J. Computer-aided diagnosis of pulmonary infections using texture analysis and support vector machine classification. *Acad. radiology* **18**, 306–314 (2011).
31. Li, L. *et al.* Using artificial intelligence to detect covid-19 and community-acquired pneumonia based on pulmonary ct: evaluation of the diagnostic accuracy. *Radiology* **296**, E65–E71 (2020).
32. Chen, J. *et al.* Deep learning-based model for detecting 2019 novel coronavirus pneumonia on high-resolution computed tomography. *Sci. reports* **10**, 1–11 (2020).
33. Wang, L., Wong, A. & Qui Lin, Z. Covid-net: A tailored deep convolutional neural network design for detection of covid-19 cases from chest x-ray images. *arXiv preprint arXiv:2003.09871* (2020).
34. Ghoshal, B. & Tucker, A. Estimating uncertainty and interpretability in deep learning for coronavirus (covid-19) detection. *arXiv preprint arXiv:2003.10769* (2020).
35. Zeiler, M. D. & Fergus, R. Visualizing and understanding convolutional networks. In *European conference on computer vision*, 818–833 (Springer, 2014).
36. Simonyan, K., Vedaldi, A. & Zisserman, A. Deep inside convolutional networks: Visualising image classification models and saliency maps. *arXiv preprint arXiv:1312.6034* (2013).
37. Mahendran, A. & Vedaldi, A. Salient deconvolutional networks. In *European Conference on Computer Vision*, 120–135 (Springer, 2016).
38. Sundararajan, M., Taly, A. & Yan, Q. Axiomatic attribution for deep networks. In *Proceedings of the 34th International Conference on Machine Learning-Volume 70*, 3319–3328 (JMLR. org, 2017).
39. Simonyan, K. & Zisserman, A. Very deep convolutional networks for large-scale image recognition. In *International Conference on Learning Representations* (2015).

40. He, K., Zhang, X., Ren, S. & Sun, J. Deep residual learning for image recognition. In *Proceedings of the IEEE conference on computer vision and pattern recognition*, 770–778 (2016).
41. Xie, S., Girshick, R., Dollár, P., Tu, Z. & He, K. Aggregated residual transformations for deep neural networks. In *Proceedings of the IEEE conference on computer vision and pattern recognition*, 1492–1500 (2017).
42. Zagoruyko, S. & Komodakis, N. Wide residual networks. *arXiv preprint arXiv:1605.07146* (2016).
43. Szegedy, C. *et al.* Going deeper with convolutions. In *Proceedings of the IEEE conference on computer vision and pattern recognition*, 1–9 (2015).
44. Huang, G., Liu, Z., Van Der Maaten, L. & Weinberger, K. Q. Densely connected convolutional networks. In *Proceedings of the IEEE conference on computer vision and pattern recognition*, 4700–4708 (2017).
45. Bengio, Y., Simard, P. & Frasconi, P. Learning long-term dependencies with gradient descent is difficult. *IEEE transactions on neural networks* **5**, 157–166 (1994).
46. Hinton, G. E., Srivastava, N., Krizhevsky, A., Sutskever, I. & Salakhutdinov, R. R. Improving neural networks by preventing co-adaptation of feature detectors. *arXiv preprint arXiv:1207.0580* (2012).
47. Szegedy, C., Vanhoucke, V., Ioffe, S., Shlens, J. & Wojna, Z. Rethinking the inception architecture for computer vision. In *Proceedings of the IEEE conference on computer vision and pattern recognition*, 2818–2826 (2016).
48. Szegedy, C., Ioffe, S., Vanhoucke, V. & Alemi, A. A. Inception-v4, inception-resnet and the impact of residual connections on learning. In *Thirty-first AAAI conference on artificial intelligence* (2017).
49. Interpretable machine learning: A guide for making black-box models explainable. <https://christophm.github.io/interpretable-ml-book> (2022). (Accessed on 15th October 2022).
50. Kopitar, L., Cilar, L., Kocbek, P. & Stiglic, G. Local vs. global interpretability of machine learning models in type 2 diabetes mellitus screening. In *Artificial intelligence in medicine: Knowledge representation and transparent and explainable systems*, 108–119 (Springer, 2019).
51. Kindermans, P.-J., Schütt, K., Müller, K.-R. & Dähne, S. Investigating the influence of noise and distractors on the interpretation of neural networks. *arXiv preprint arXiv:1611.07270* (2016).
52. Springenberg, J. T., Dosovitskiy, A., Brox, T. & Riedmiller, M. Striving for simplicity: The all convolutional net. *arXiv preprint arXiv:1412.6806* (2014).
53. Shrikumar, A., Greenside, P. & Kundaje, A. Learning important features through propagating activation differences. In *Proceedings of the 34th International Conference on Machine Learning-Volume 70*, 3145–3153 (JMLR. org, 2017).
54. Krug, A., Knaebel, R. & Stober, S. Neuron activation profiles for interpreting convolutional speech recognition models. In *NeurIPS Workshop IRASL: Interpretability and Robustness for Audio, Speech, and Language* (2018).
55. Krug, A., Ebrahimzadeh, M., Alemann, J., Johannsmeier, J. & Stober, S. Analyzing and visualizing deep neural networks for speech recognition with saliency-adjusted neuron activation profiles. vol. 10, 1350 (Multidisciplinary Digital Publishing Institute, 2021).
56. Krug, A., Ratul, R. K. & Stober, S. Visualizing deep neural networks with topographic activation maps. *arXiv preprint arXiv:2204.03528* (2022).
57. Paszke, A. *et al.* Pytorch: An imperative style, high-performance deep learning library. In Wallach, H. *et al.* (eds.) *Advances in Neural Information Processing Systems 32*, 8024–8035 (Curran Associates, Inc., 2019).
58. Kokhlikyan, N. *et al.* Captum: A unified and generic model interpretability library for pytorch (2020). [2009.07896](https://arxiv.org/abs/2009.07896).
59. Chatterjee, S. *et al.* TorchEsegeta: Framework for Interpretability and Explainability of Image-based Deep Learning Models. *Appl. Sci.* **12**, 1834, DOI: [10.3390/app12041834](https://doi.org/10.3390/app12041834) (2022).
60. Kingma, D. P. & Ba, J. Adam: A method for stochastic optimization. *arXiv preprint arXiv:1412.6980* (2014).
61. Pytorch reproducibility. <https://pytorch.org/docs/stable/notes/randomness.html>. (Accessed on 31st May 2020).
62. Nvidia apex. <https://github.com/NVIDIA/apex>. (Accessed on 31st May 2020).
63. Covid-19 image data collection. <https://github.com/ieee8023/covid-chestxray-dataset>. (Accessed on 31st May 2020).
64. Kermany, D., Zhang, K. & Goldbaum, M. Labeled optical coherence tomography (oct) and chest x-ray images for classification. *Mendeley data* **2** (2018).
65. Chest x-ray images (pneumonia). <https://www.kaggle.com/paultimothymooney/chest-xray-pneumonia>. (Accessed on 31st May 2020).

66. Radiopaedia: Chest radiograph. <https://radiopaedia.org/articles/chest-radiograph?lang=us>. (Accessed on 31st May 2020).
67. Diamond, M., Peniston, H. L., Sanghavi, D., Mahapatra, S. & Doerr, C. *Acute Respiratory Distress Syndrome (Nursing)* (StatPearls Publishing, Treasure Island (FL), 2021).
68. Matthay, M. A. *et al.* Acute respiratory distress syndrome. *Nat. reviews Dis. primers* **5**, 1–22 (2019).
69. Fan, E. *et al.* Covid-19-associated acute respiratory distress syndrome: is a different approach to management warranted? *The Lancet Respir. Medicine* **8**, 816–821 (2020).
70. Gattinoni, L., Chiumello, D. & Rossi, S. Covid-19 pneumonia: Ards or not? (2020).
71. Bain, W. *et al.* Covid-19 versus non-covid-19 acute respiratory distress syndrome: comparison of demographics, physiologic parameters, inflammatory biomarkers, and clinical outcomes. *Annals Am. Thorac. Soc.* **18**, 1202–1210 (2021).
72. Tsoumakas, G. & Katakis, I. Multi-label classification: An overview. *Int. J. Data Warehous. Min. (IJDWM)* **3**, 1–13 (2007).
73. Charte, F., Rivera, A. J., del Jesus, M. J. & Herrera, F. Addressing imbalance in multilabel classification: Measures and random resampling algorithms. *Neurocomputing* **163**, 3–16 (2015).
74. Denise E. Morris, D. W. C. & Clarke, S. C. Secondary bacterial infections associated with influenza pandemics. *Front. Microbiol.* (2017).
75. Shigeo Hanada, K. Y. C., Mina Pirzadeh & Deng, J. C. Respiratory viral infection-induced microbiome alterations and secondary bacterial pneumonia. *Front. Immunol.* (2018).
76. Ribeiro, M. T., Singh, S. & Guestrin, C. " why should i trust you?" explaining the predictions of any classifier. In *Proceedings of the 22nd ACM SIGKDD international conference on knowledge discovery and data mining*, 1135–1144 (2016).
77. Lundberg, S. M. & Lee, S.-I. A unified approach to interpreting model predictions. In *Advances in neural information processing systems*, 4765–4774 (2017).



COVID-19

**Figure 7.** Comparison of various interpretability techniques with respect to models for COVID-19 predictions against the manual annotation of the affected areas by medical experts.



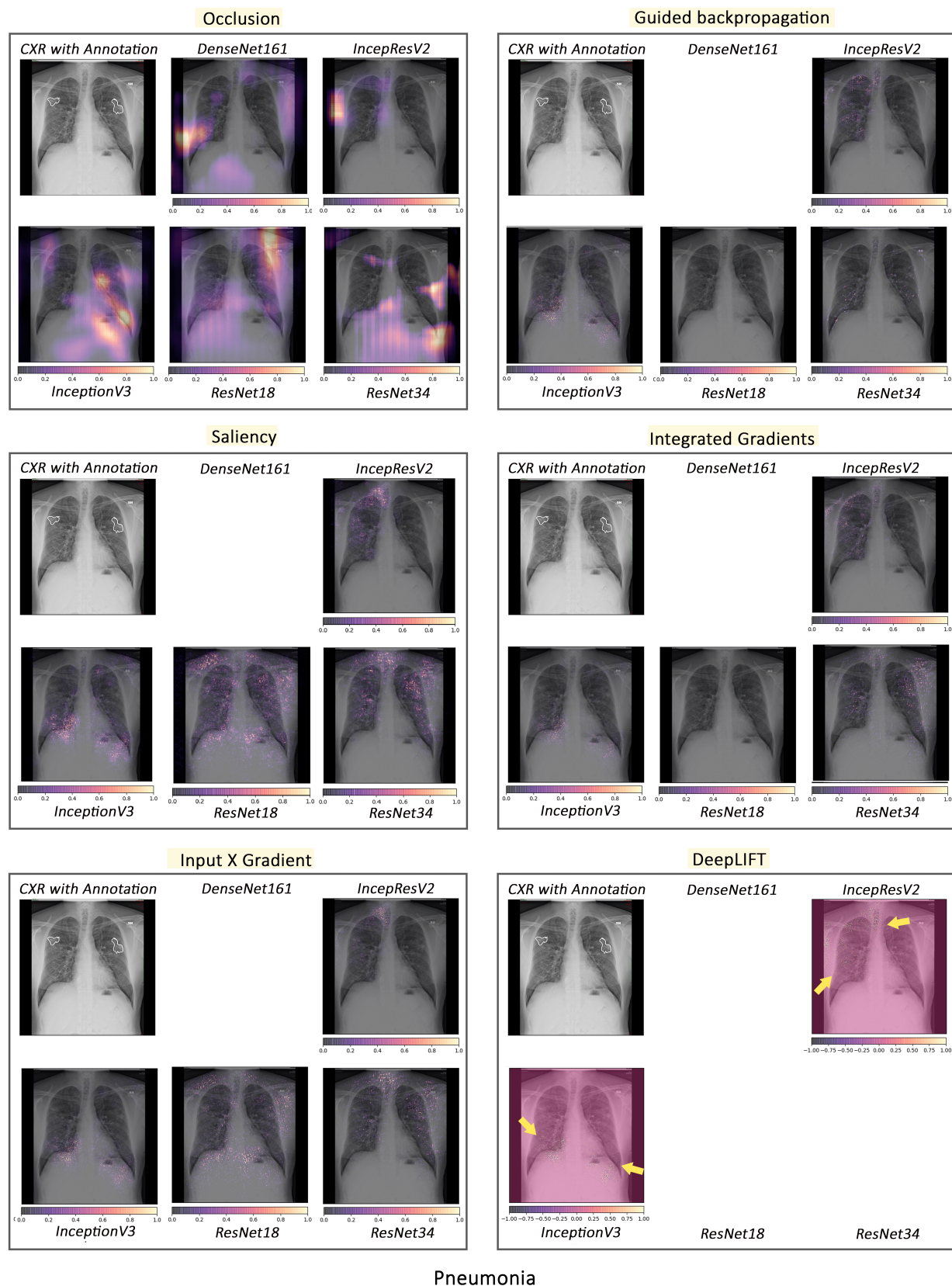


**Figure 8.** Comparison of various interpretability techniques with respect to models for pneumonia predictions against the manual annotation of the affected areas by medical experts.





**Figure 9.** Comparison of various interpretability techniques with respect to models for viral pneumonia predictions against the manual annotation of the affected areas by medical experts.

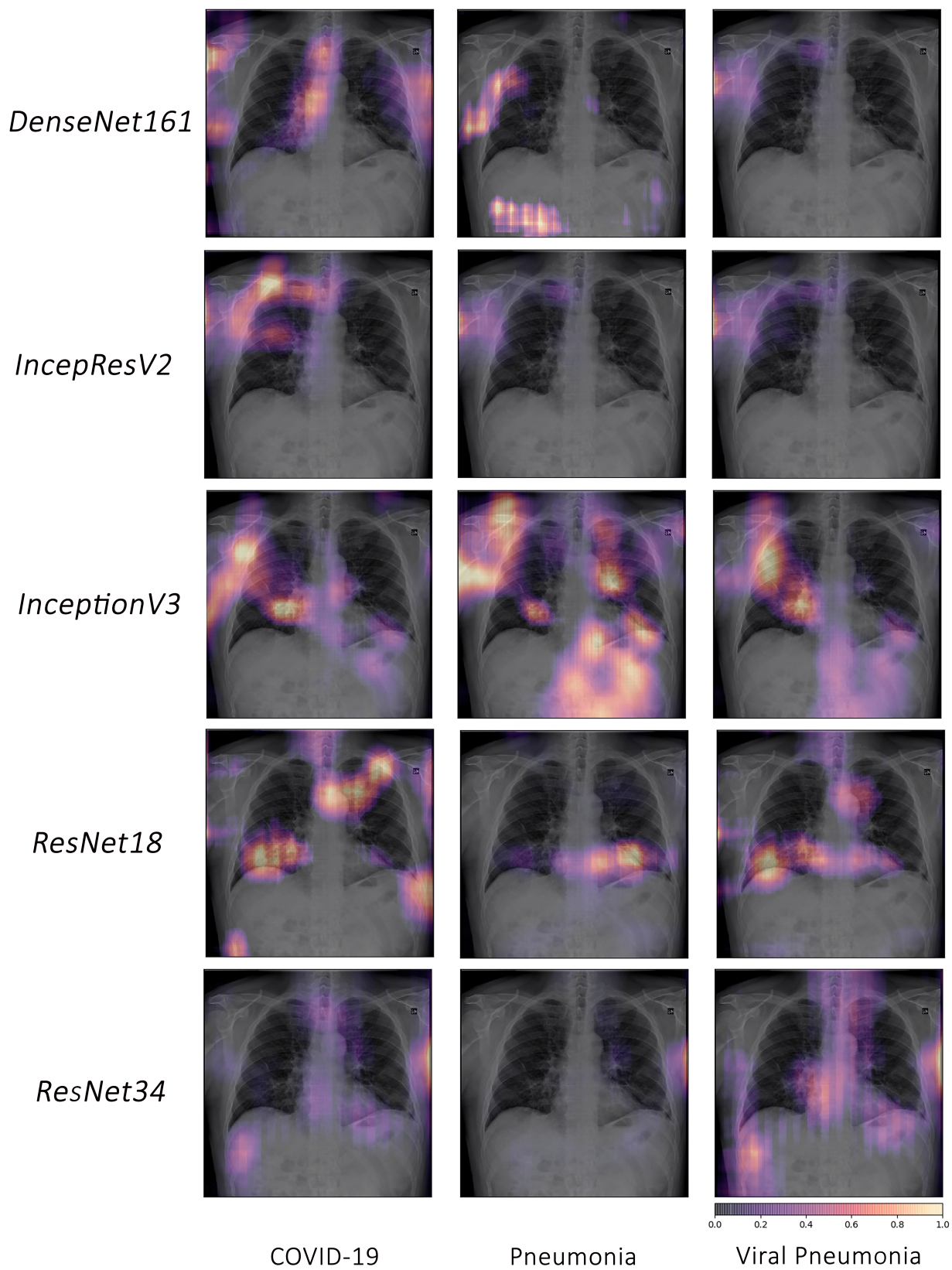


**Figure 10.** Example of occlusion for lung pathologies: COVID-19, pneumonia and viral pneumonia